ANNEX E. -TABLE OF CONTENTS

ANNEX E. Bio-optical characteristics of Lampedusa area

The bio-optical characterization of Lampedusa test site is here performed using in situ observations acquired by the CNR during a dedicated cruise in the area (the Sentinel-3 cruise) during June 2017, and by analysing the data continuously collected by the optical buoy (Meda) located 3 miles off shore the island. To this end, radiometric and inherent optical property (IOP) data along with more common standard oceanographic measurements (temperature, salinity, fluorimeter-derived phytoplankton chlorophyll concentration and coloured dissolved organic matter) are presented.

1 Data and methods

1.1 Radiometry

Among the objectives of using the in situ radiometric measurements is to derive surface, above-water Rrs spectra from in-water measurements. Here, we use both data collected from a profiling system and from the radiometers mounted at fixed depths over the Meda optical buoy (Figure 8).
Apart from the integration depth (see below) which may vary for data acquired using the profiler but not for those on the buoy, data processing is identical for the two datasets. Radiometers are those from the Satlantic Inc. (OCR-507) and are made for measuring the upwelling radiance (L_u) the downward and the upward irradiance (E_d and E_u) and includes a reference sensor for the downward irradiance (E_s), mounted on the uppermost and undisturbed deck of the ship or of the buoy. The profiler is equipped with a Sea-bird CTD and a tilt sensor.
The radiometric measurements are acquired and processed following the method described in Zibordi et al. (2011). To increase the number of samples per unit depth, data are acquired using the multicast technique (D'Alimonte et al., 2010; Zibordi et al., 2004). Multi-level data processing is achieved using the Software for the Elaboration of Radiometer Data Acquisitions (Volpe et al., 2019), developed at the Institute of Marine Science in Rome, Italy. The processing steps follow the consolidated protocols for data reduction of in-water radiometry (Mueller and Austin, 1995; Zibordi et al., 2011). First, data are converted from digital counts into their physical units. A filter is applied to remove data with profiler tilt angle larger than 5°. In order to reduce the influence of the light variability during the measurements, data from each sensor are normalised by the above-water downwelling irradiance. A least-square linear regression is performed on the log-transformed normalised data, whose slope determines the diffuse attenuation coefficients of spectral upwelling radiance (K_L), spectral upwelling irradiance (K_U) and spectral downwelling irradiance (K_d); the exponents of the intercepts are the spectral sub-surface quantities ($L_u(0-, \lambda)$, $E_u(0-, \lambda)$ and $E_d(0-, \lambda)$). Outliers due to wave perturbations are removed and identified in those points differing, by default, more than two standard deviations from the regression line. The depth layer normally considered as relevant for the extrapolation to the surface is 0.3-3 m, but can be changed on the basis of the characteristics of each profile. The upwelling sub-surface quantities (i.e. $L_u(0-, \lambda)$, $E_u(0-, \lambda)$) are also corrected for the self-shading effect following Zibordi and Ferrari (1995) and Mueller and Austin (1995) using the ratio between diffuse and direct atmospheric irradiance, and the sea-water absorption. Using the primary sub-surface quantities, it is then possible to derive additional products such as the Q-factor at nadir ($Q_n(0^-,\lambda)=E_u(0^-,\lambda)/L_u(0^-,\lambda)$), the remote sensing reflectance ($Rrs(\lambda)=0.543 \cdot L_u(0-,\lambda)/E_s(0,\lambda)$) or the normalized water-leaving radiance ($L_{wn}(\lambda)=Rrs(\lambda) \cdot E_0(\lambda)$ with $E_0(\lambda)$ being the extra-atmospheric solar irradiance; Thuillier et al., 2003).

1.2 Inherent Optical Property

IOPs are essential properties of the ocean and are here used to characterize the area of Lampedusa. IOPs include absorption (a), scattering (forward, b_f, and backward, b_b) and attenuation, which is the sum of the first two, of light by particles into the water. Hyperspectral absorption and attenuation at visible wavelengths were measured with a Wetlabs AC-s meter while backscattering was measured with an ECO-VSF3 also from Wetlabs. Both instruments were shipped for factory calibration before the campaign and were not utilized until then, thus minimizing drift with time. For in-situ measurements, the IOP package containing the ECO-VSF3, the AC-s meter and a Seabird CTD was submerged with a mechanical winch located at one side of the ship.

AC-s data are corrected following standard NASA recommendations, including correction for differences in temperature and salinity, drift correction and residual scatter of the absorption tube correction (Pegau et al. 2003).

The ECO-VSF3 measures the volume scattering function at three wavelengths (470, 532 and 660 nm) and in three nominal angles (100°, 125° and 150°); a more in depth analysis demonstrated that the three angles are 111°, 138° and 154° (Michael Twardowski, personal communication). Backscattering is calculated by angular integration (Pitarch et al., 2016). To approximate this integral, ECO-VSF3 measurements are weighted by sin θ (111°, 138° and 154°) and fitted to a 3rd degree polynomial that is forced to be zero at 180°. The polynomial is extrapolated until 90° and then integrated. These calculations are done automatically by the processing software which also provides the VSF at the three angles and three bands. Contrary to the case of radiometry, b_b measurements have lacked a solid amount of studies on cross-calibration and uncertainty assessment. In this absence, we follow recent results comparing VSF between ECO-VSF and hyperangular meter MASCOT, with a maximum reported discrepancy of 5 % (Sullivan et al., 2013).

2 Results

2.1 Sentinel-17 Cruise

2.1.1 Oceanography

The area around Lampedusa (Figure 1) was sampled during two consecutive days on the 3 and 4 June, 2017. Oceanographically, the area presents a seasonal mixed layer down to ~15 meters likely driven by surface heating and light winds and a more homogeneous layer down to 50 meters (Figure 2b,c). These two layers, together, are the Modified Atlantic water (MAW) and are clearly visible in the T-S diagram (Figure 2a) as the layer characterized by roughly constant salinity (~37.25 psu) as compared with the more pronounced temperature gradient of 5°C (17°C to 22°C). The deeper layer (65 m – bottom) is characterized by the presence of saltier waters, most probably originated by the interaction between the surface waters from the western basin (Malanotte-Rizzoli et al., 1997) and the intermediate waters from the Levantine basin (Roether et al., 1998). This layer is characterized by roughly constant or slowly decreasing temperature (16°C to 15°C) and a larger salinity gradient (from 37.2 psu to 37.9 psu, Figure 2a-c).

2.1.2 Bio-optics

The average chlorophyll profile reflects this variability with low and nearly invariant values in the surface layers (down to 50 m depth) and higher values towards the bottom. Moreover, it is worth mentioning that despite the short time between the first (7 UTC 3 June, 2019) and the last cast (12 UTC 4 June, 2019), the area appears quite stable in all its aspects, oceanographically and biologically. This is also true when observing the area from the optical point of view. Figure 3d shows the coefficient of variation (average over the standard deviation) versus depth of the back scattering coefficient as derived from the integration of the Volume Scattering Function in three wavelengths and three angles (http://www.comm-tec.com/Prods/mfgs/Wetlabs/Manuals/Eco-VSF3_manual.pdf). To easy the interpretation and for coherence with the ECO-VSF3 measurements, the three bands are also extracted for the absorption and attenuation coefficients, for which the coefficient of variation is also computed and plotted against the depth (Figure 3e,f). The variability of these three parameters is consistent with the oceanographic picture given above, with the first layers showing lower values (not shown) and variability than those in the deeper layer. It is interesting to note that such low variability is also visible in the b_b slope (Figure 4), highlighting that the water constituents are homogeneously distributed along the water column and that the surface values are fairly representative of the upper ~50 meters. Moreover, Figure 3 also shows that the variability of the light attenuation in the upper layer is mostly driven by the absorption while the back scattering plays a role mostly in the deeper layer. The backscattering values observed here are consistent with those observed in clear and very clear waters, globally (Huot et al., 2008; Brewin et al., 2012).

Figure 5 shows the average and standard deviation profiles of E_d and L_u. The single profiles were first individually binned over depth at 0.5 meter resolution. These profiles were then averaged together so that the low variability in the surface actually reflects the space-time homogeneity of the field. From the remote sensing point of view, Figure 6 shows that the remote sensing reflectance is a quite stable quantity (across the two days and over roughly 3000 squared km, the area shown in Figure 1), only varying of a few percent's over the entire spectrum. The coefficient of variation computed from the k_d spectra shows much larger variability then those exhibited by the Rrs. This is largely given by the fact that K_d is very sensitive not only to the water transparency and water constituents but also on the sea state, which, through the lensing effect, induces orders of magnitude variability in the E_d estimation from which K_d is computed by fitting E_d with depth.
Figure 7 shows the closure experiment between measured Rrs (from radiometric data as shown in Figure 6a) and the one derived using IOPs observations. IOP-derived Rrs is computed according to:

$$Rrs = \frac{f}{Q}\Re\frac{b_b}{a+b_b},$$

with the f/Q factor being equal to 0.11 and the dimensionless factor, $\Re$, being 0.53 (Morel et al., 2002). The closure experiment demonstrates the high internal data consistency and quality with differences between the two estimates not exceeding 4%. To evaluate the impact of the pure seawater contribution (taken from Zang et al., 2019) to the overall goodness of the closure experiment, the pure seawater theoretical Rrs spectrum in Figure 7 is also shown.

2.2 Meda

2.2.1 Oceanography

This section describes the analysis of the data collected by the instrumentation mounted on the Meda buoy (Figure 8). The temporal coverage of the instrumentation varies from more than one year for the deepest sensors (CTD, and O_2 sensor) to a few months for radiometry. Figure 9 shows the monthly aggregated T-S diagram using the CTD observations at 18 meters. A seasonal cycle is clearly evident with the summer months characterized by warmer and saltier waters. It can be seen that the spring 2019 was as cool as the end of autumn-beginning of winter; this led June 2019 to be as much as five degrees Celsius cooler than June 2018. In July 2019 the water temperature was not significantly different than the one measured one year earlier, in July 2018; however, salinity showed a remarkable increase from both June 2019, which was characterized by high variability, and as compared to July 2018. This is likely given either by a strong mixing event in which warmer and saltier surface water (the so-called Mediterranean Mixed Water, Ben Ltaief et al. 2015) deepens to depth or by horizontal advection of MMW. Figure 10a shows the temperature annual cycle measured at 1 meter depth spanning 15°C (black line labelled on right vertical axis) and with a daily cycle not exceeding ± 3% from the average daily value. The daily oscillation is larger in summer.

2.2.2 Bio-optics

Figure 10b-d shows the daily cycle anomalies of the fluorescence-derived phytoplankton chlorophyll concentration (chl), volume scattering function (VSF) and of the coloured dissolved organic matter (CDOM)

at 4.5 meters depth. In line with the current knowledge (Volpe et al., 2019), chl annual cycle presents a peak in winter and a daily minimum in correspondence of the highest illumination conditions (Figure 10b). The latter pattern is consistent with the intracellular photoacclimation process and the packaging effect (Volpe et al., 2012; Bellacicco et al., 2016). The phytoplankton annual cycle is also evident in the VSF and CDOM cycle (Figure 10c-d) with maxima in winter and lower values at summertime. Seasonality is further shown by the distribution histograms of Figure 11, in which it is shown that chl exceeds the 0.1 mg m^{-3} threshold only 30% of the time (black line) mostly due to winter conditions (green line).
As already shown in Figure 6a, the Rrs spectra present a maximum in the blue band at 412, a band which is not part of the set of bands operationally used to retrieve the chlorophyll concentration from space over the Mediterranean Sea (Volpe et al., 2019). When this band (412 nm) is not used to derive the maximum band ratio to compute chlorophyll there is an overestimation of chlorophyll at low values (not shown). The use of the 412 band in the chlorophyll algorithm improves the retrieval and is shown in Figure 12.

2.3 Satellite Observations

2.3.1 Ocean colour remote sensing

Figure 13a shows the average map of the chlorophyll concentration at basin scale which put in light its general oligotrophic nature and with both horizontal (west to east) and meridional (north to south) gradients. Lampedusa and Antikythera are on average below 0.1 mg m^{-3} (the threshold suggested by Zibordi et al. (2017) as the characteristics for system vicarious calibration sites), while Boussole appears to be above. The short scale system variability is represented by the average day-to-day percent difference (Figure 13b). The southern candidate sites display lower variability than Boussole, which is also subject to a higher longer scale variability as shown in Figure 13c.

2.3.2 Sea Surface Temperature

Figure 14a shows the SST yearly average (2013) for the entire Mediterranean Sea, from which a clear northwest-southeast of increasing gradient is recognizable. Lampedusa shows an average surface temperature of 21°C, which is analogous to Antikythera and significantly higher than the Boussole site (17°C). The seasonal variability of Lampedusa is larger than that of Antikythera; this is reasonably due to the shallower bathymetry of the Sicily Channel as compared to that of the Antikythera area. Boussole site shows the higher seasonal variability among the three sites (Figure 14b), due to the high oceanographic dynamics of the area seasonally subject to deep mixing. In general, the short-term variability of the northwestern sector and in particular of the Liguro-provençal area is higher being dominated by larger dynamics as shown by Figure 14c; on the other hand, at this temporal scale, Lampedusa site appears quite stable as much as Antikythera.

3 Figures

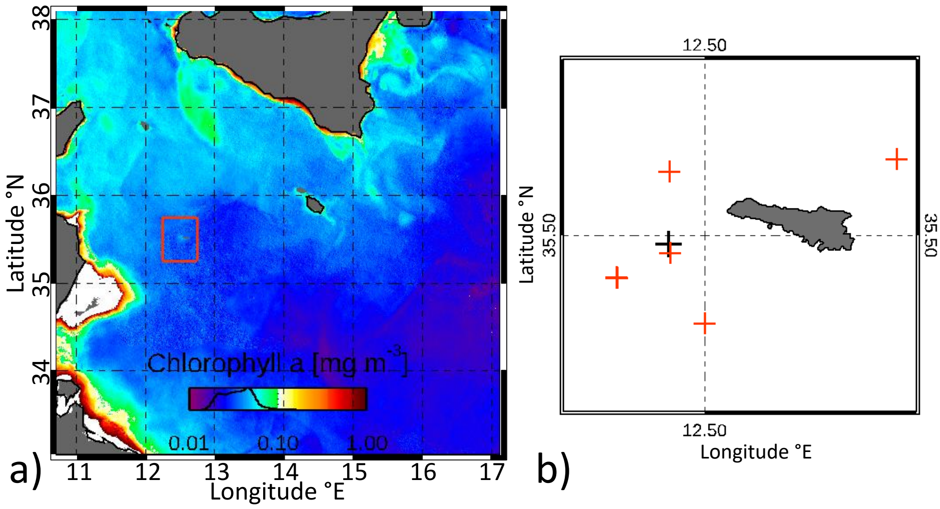

Figure 1 Daily Level-4 chlorophyll (OCEANCOLOUR_MED_CHL_L4_NRT_OBSERVATIONS_009_041) from the Copernicus Marine Environment Monitoring Service archive for June 3, 2017 (panel a). The red square locates the sampling area shown in panel b. Red crosses indicate the location of the seven casts performed during the Sentinel-17 cruise around Lampedusa on the third and fourth June, 2017. The location of the Meda buoy is marked in black.

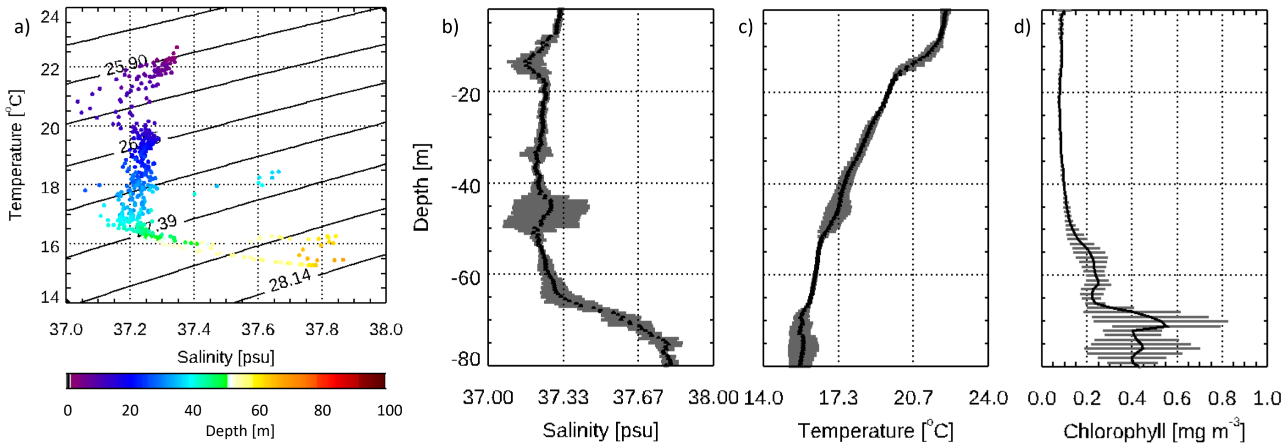

Figure 2 panel a – temperature-salinity diagram for the seven CTD casts shown in Figure 1; continuous oblique lines are the isopycnals. Each T-S measurement is color-coded according to the depth. The average (black line) and standard deviation (grey shaded) profiles of salinity (b), temperature (c) and phytoplankton chlorophyll *a* concentration (d) are also shown.

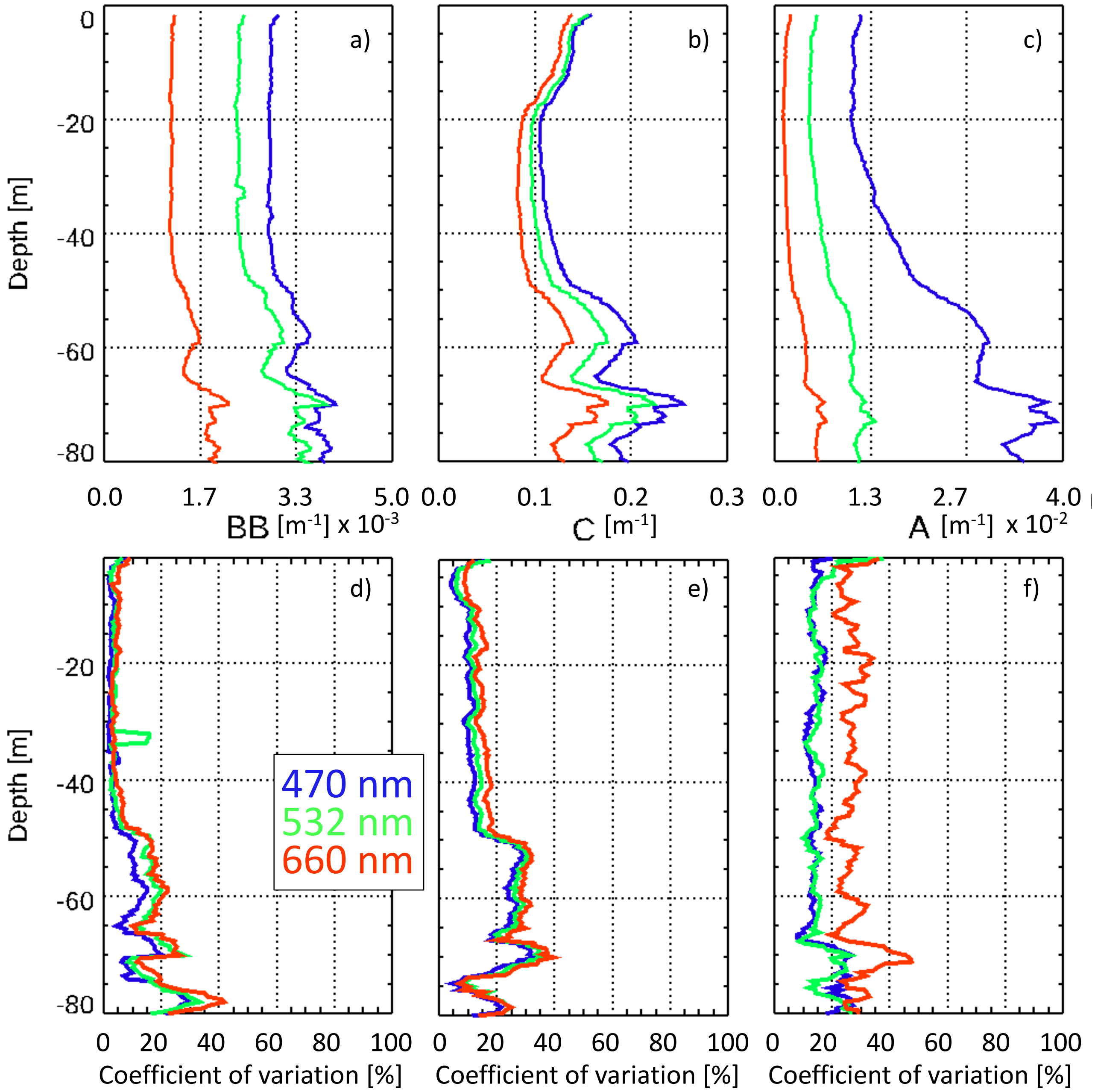

Figure 3 Average profiles of backscattering (panel a), attenuation (panel b) and absorption (panel c) coefficients. Coefficient of variation versus depth for the back-scattering coefficient derived from the ECO-VSF3 casts (d). The coefficient of variation for the attenuation (e) and absorption (f) coefficients has been computed for the same three bands as the b_b.

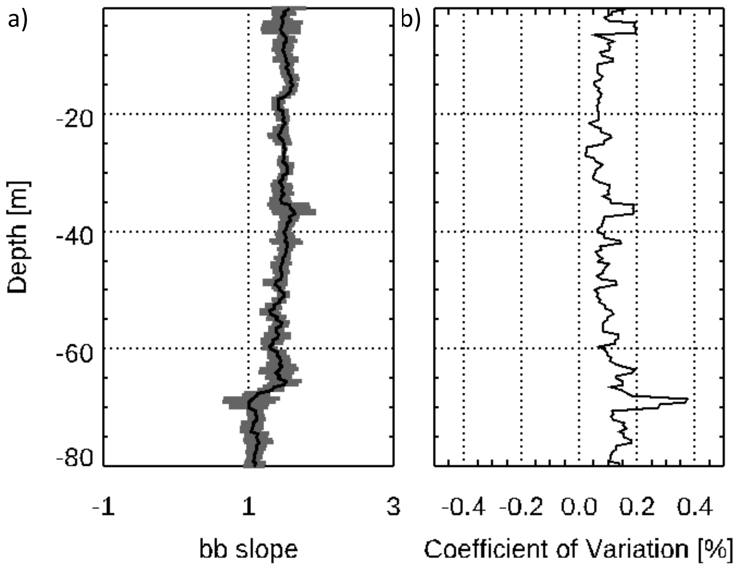

Figure 4: back-scattering slope (left) and its coefficient of variation (right) profiles.

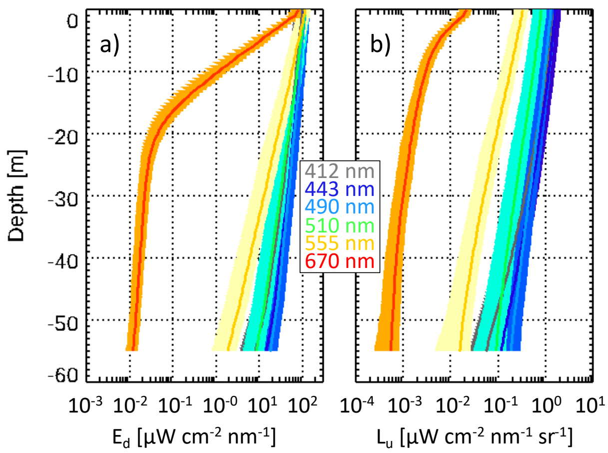

Figure 5 Average profiles of spectral downwelling irradiance (panel a) and upwelling radiance (panel b) for the 6 bands of the Satlantic profiler. Shaded areas are the plus or minus one standard deviation.

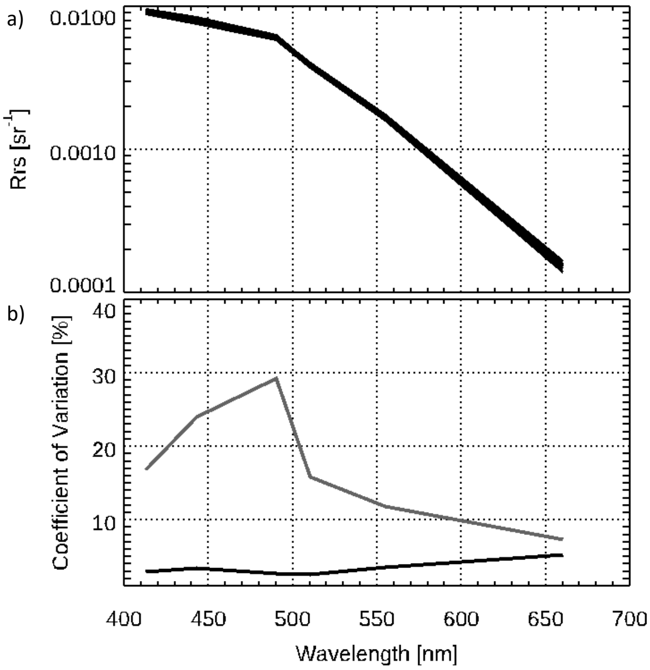

Figure 6 Remote sensing reflectance spectra (upper panel) from the seven casts shown in Figure 1. Coefficient of variation of the Rrs and of the attenuation coefficient of light (lower panel).

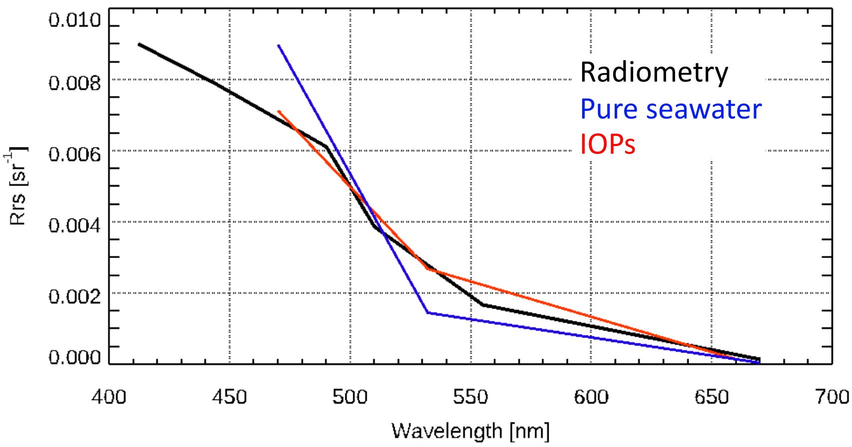

Figure 7 Closure experiment between measured Rrs (from radiometric data as shown in Figure 6a) and IOPs observations as shown in Figure 3. As reference, the theoretical Rrs due to pure seawater is also included (blue line).

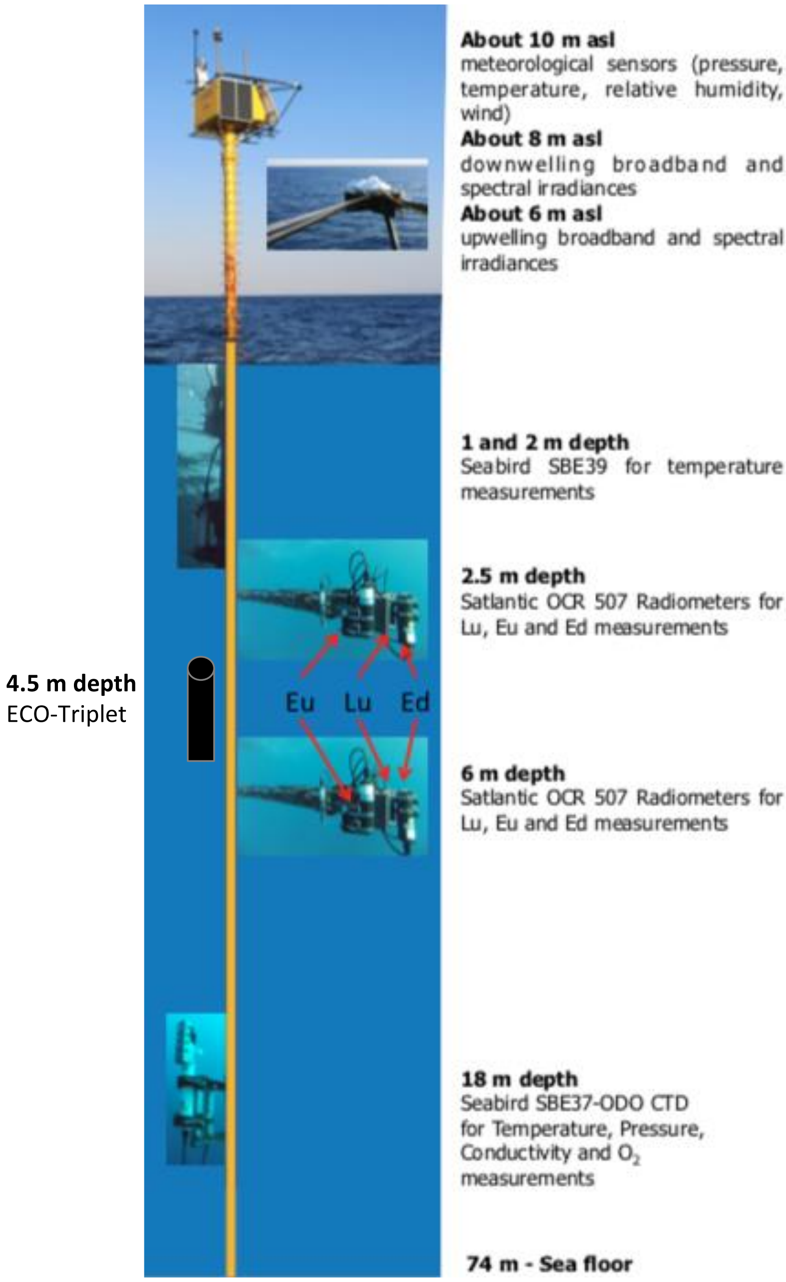

Figure 8 global picture of the Meda buoy instrumentation and their vertical distribution: at 10 m (above mean sea level) meteorological sensors to measure pressure, air temperature, relative humidity and wind. Radiometers to measure downwelling broadband and spectral irradiance are located at 8 m, while those for the upwelling (broadband and spectral) irradiance are located at 6 m. Two thermometers Seabird SBE39 are located at 1 and 2 meters depth, respectively. Two sets of Satlantic OCR 507 radiometers for upwelling radiance and irradiance and downwelling irradiance are located at 2.5 m and 6 m depth. The ECO-Triplet for measuring phytoplankton chlorophyll concentration, volume scattering function at 532 nm and coloured dissolved organic matter is located at 4.5 meters depth. The fluorescence signal at 460 nm and 695 nm is used to estimate the CDOM and the chlorophyll concentration. At 18 meter depth, a Seabird SBE37-ODO CTD is used to measure conductivity, temperature, pressure and oxygen concentration.

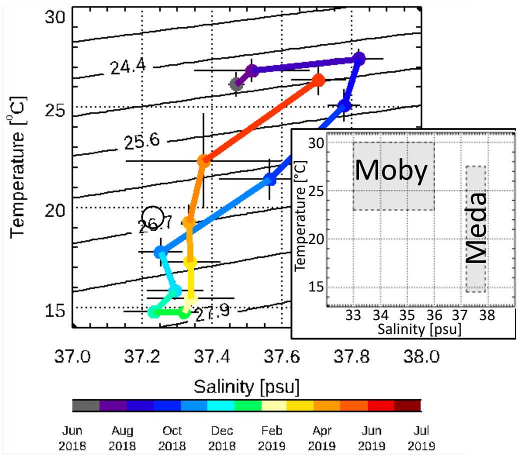

Figure 9: Meda buoy – T-S diagram using the CTD at 18 m depth. Values are colour-coded according to time of measurement. The pink circle corresponds to the T-S values measured in June 2017, during the Sentinel-17 cruise and shown in Figure 2a. Superimposed is a plot showing the Temperature and Salinity ranges of variability of the Lampedusa Meda buoy in comparison with those of Marine Optical Buoy (MOBY, Feinholtz et al., 2017).

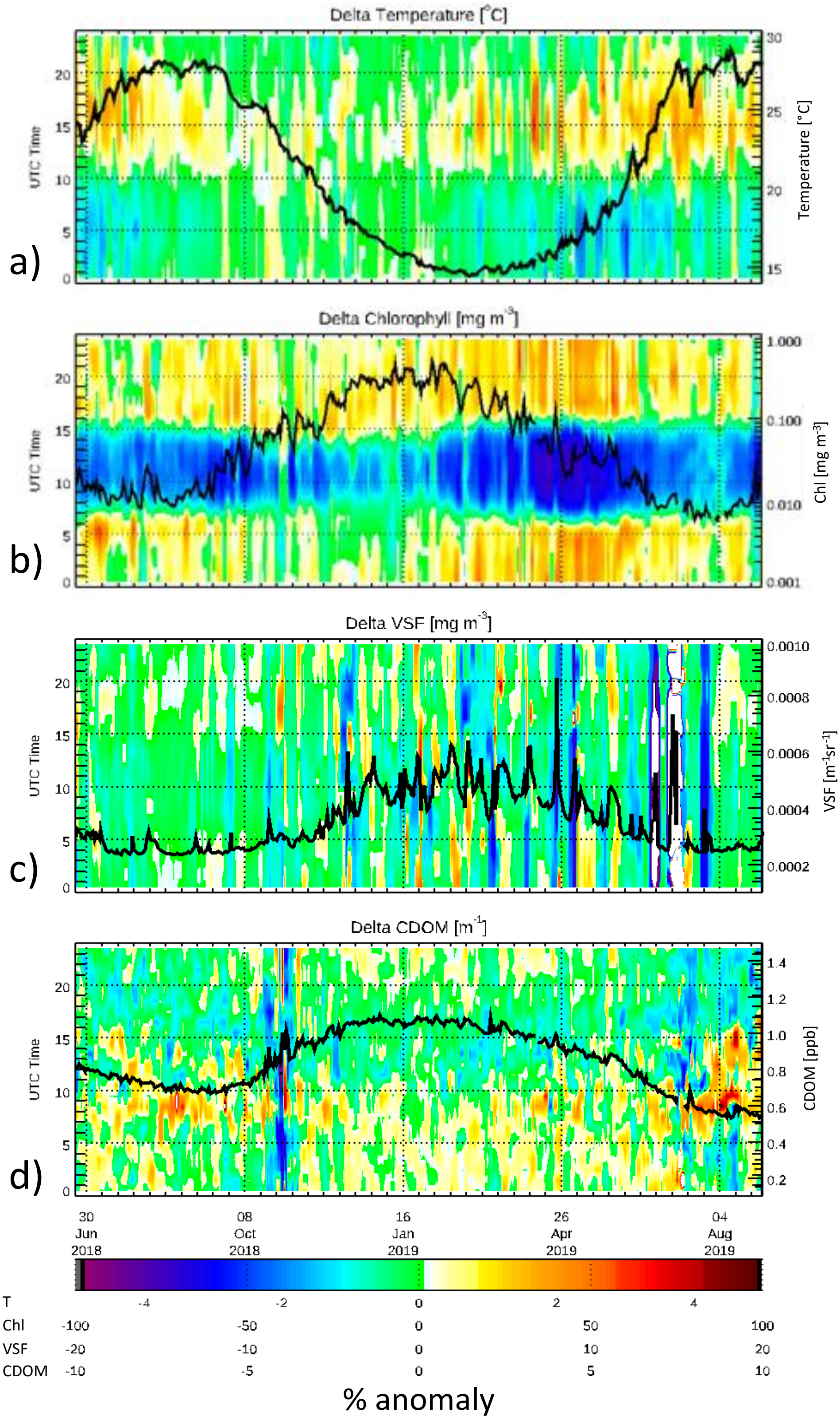

Figure 10: anomaly time series of chlorophyll concentration (panel a), sea water temperature (panel b), volume scattering function (panel c) and coloured dissolved organic matter (panel d). The difference between the daily values and their average (over plotted as black line in each panel) is then divided by the mean value itself, for

normalization. The normalized values are expressed as percent values. The temperature sensor is the one located at 1 meter depth.

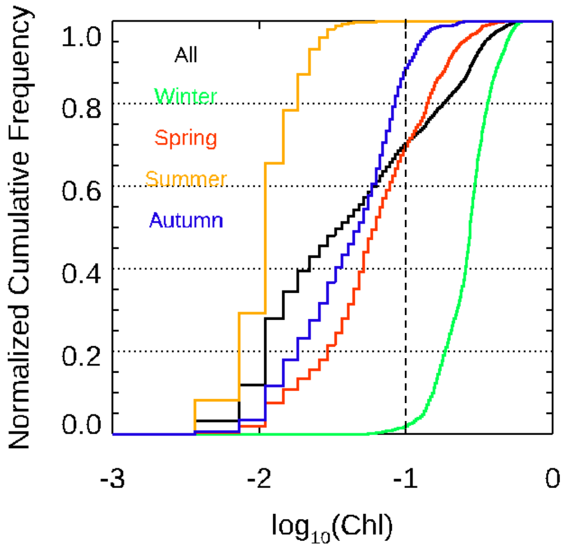

Figure 11: Normalized cumulative distribution of the log_{10}-transformed chlorophyll concentration measured at 4.5 meter depth. Different colours indicate seasons, while the dashed line represents the 0.1 mg m^{-3} threshold as defined in Zibordi et al. (2017).

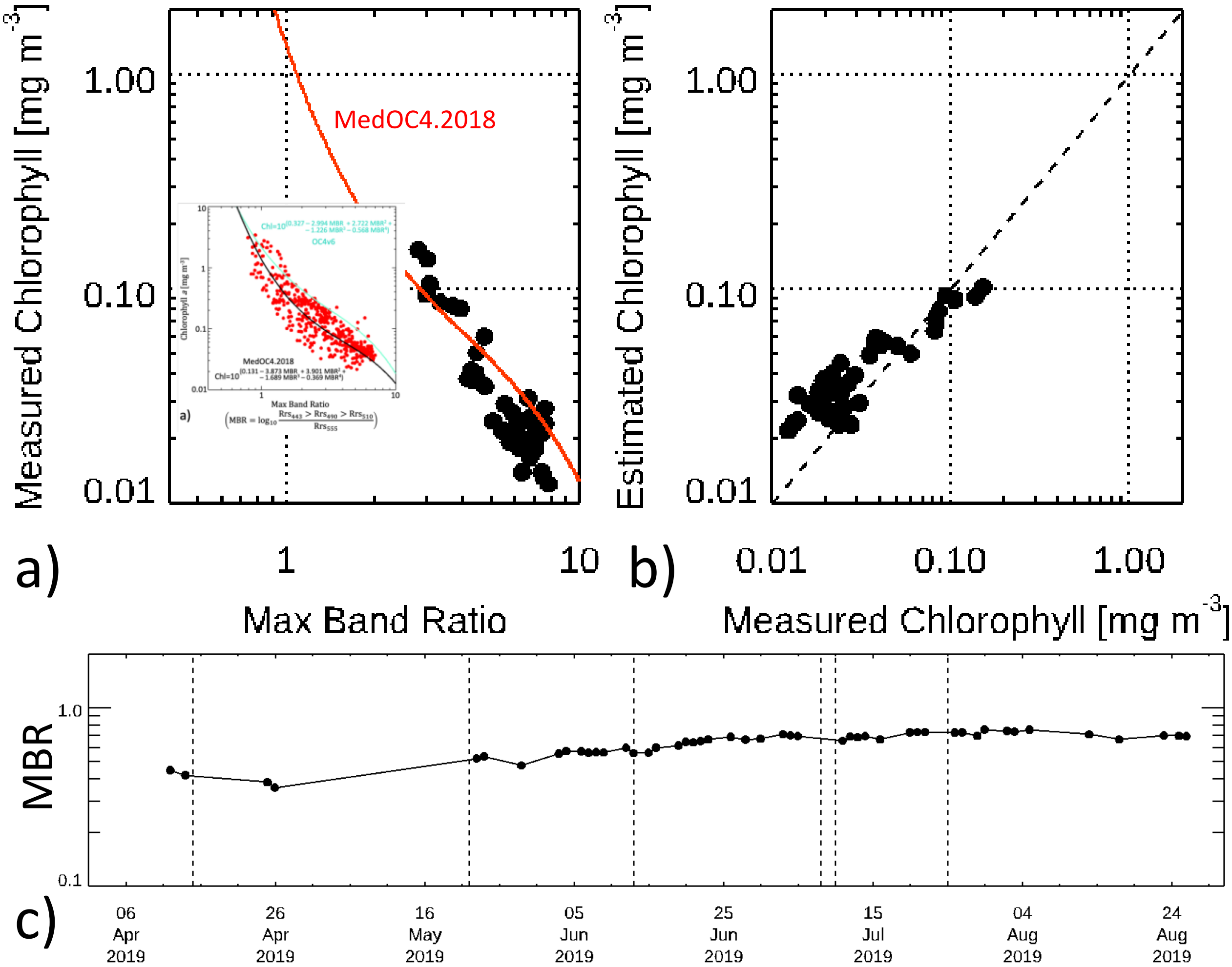

Figure 12: Panel a – fluorescence-derived chlorophyll as function of the maximum band ratio computed as the ratio between the maximum Rrs value among those at 412, 443, 490, and 510 nm and that at 555 nm. The red line is the MedOC4.2018 functional form, which is derived from the red dots in the inlet plot, which in turn is adapted from Figure 6a of Volpe et al. (2019). Panel b is the measured fluorescence-derived chlorophyll and the one estimated via MedOC4.2018. Panel c shows the maximum band ratio time series. The vertical dashed lines indicate the days of maintenance. Missing data are the result of the data screening.

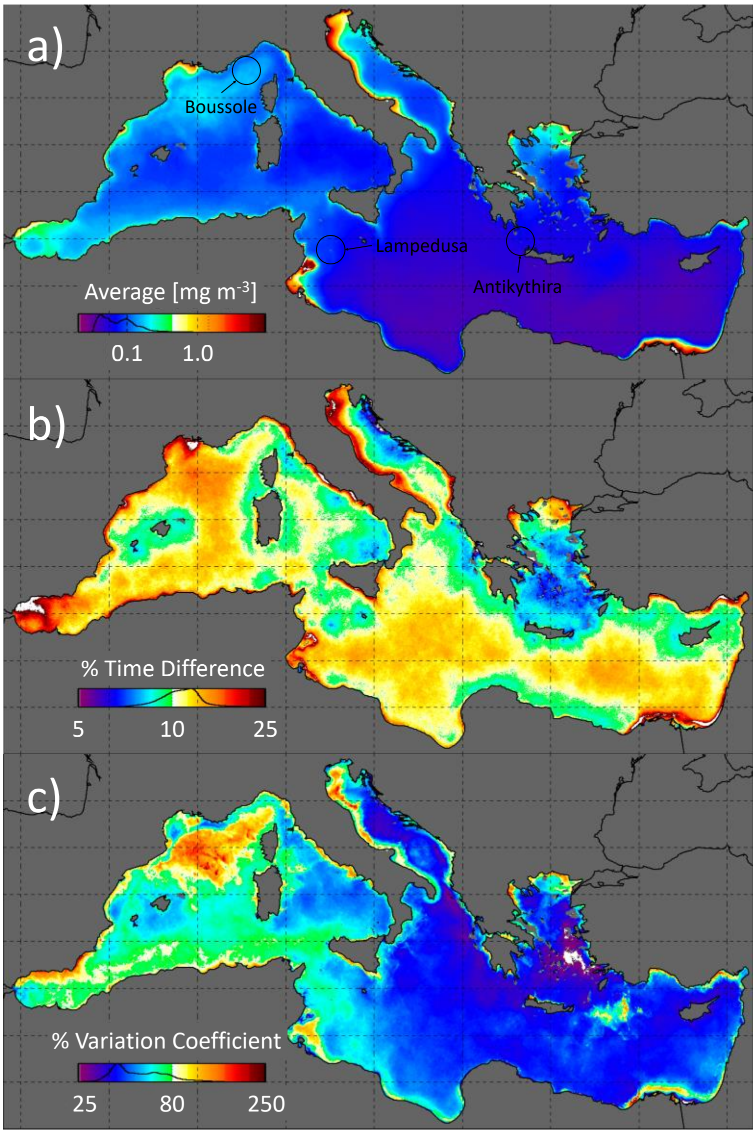

Figure 13: Panel a – average of phytoplankton chlorophyll concentration as derived from the daily Level-4 (OCEANCOLOUR_MED_CHL_L4_NRT_OBSERVATIONS_009_041) product from the Copernicus Marine Environment Monitoring Service archive from January 2017 to September 2019. Panel b – pixel-scale average temporal difference (percent) computed by averaging the day-to-day anomalies over the same period as panel a. Panel c – pixel-scale coefficient of variation computed as the time series standard deviation over its mean value over the same period as panel a.

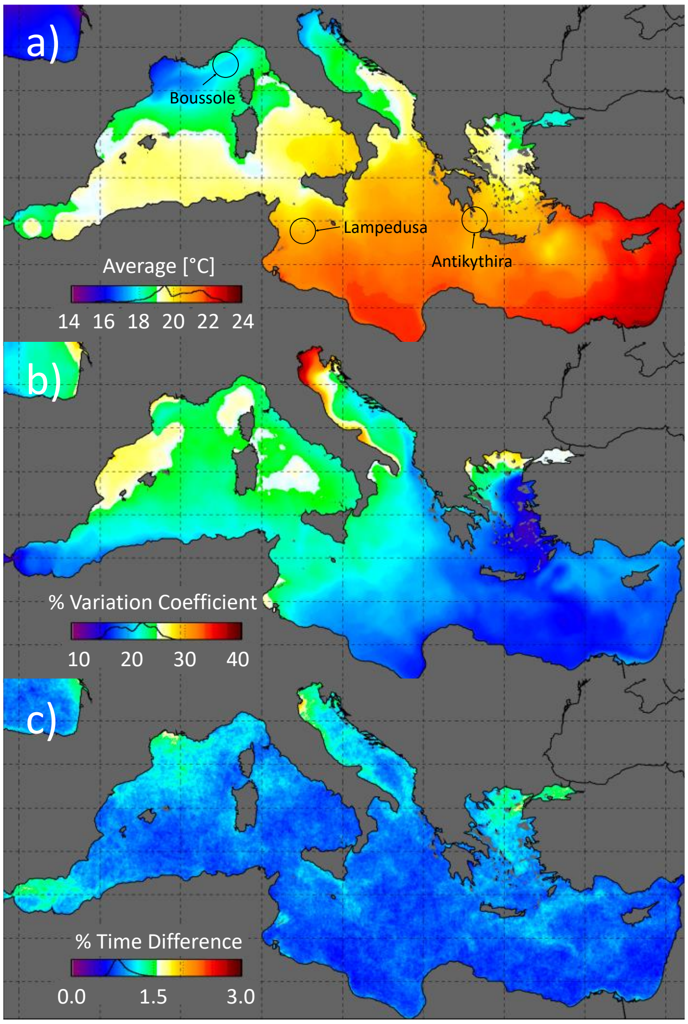

Figure 14: Panel a – average of sea surface temperature (Celsius Degrees) as derived from the daily Level-4 (SST_MED_SST_L4_NRT_OBSERVATIONS_010_004) product from the Copernicus Marine Environment Monitoring Service archive for the reference year 2013. Panel b – pixel-scale coefficient of variation computed as the time series standard deviation over its mean value over the same period as panel a. Panel c – pixel-scale average temporal difference (percent) computed by averaging the day-to-day anomalies over the same period as panel a.

4 References

Bellacicco, M., Volpe, G., Colella, S., Pitarch, J., Santoleri, R., 2016. Remote Sensing of Environment In fl uence of photoacclimation on the phytoplankton seasonal cycle in the Mediterranean Sea as seen by satellite. Remote Sens. Environ. 184, 595–604. https://doi.org/10.1016/j.rse.2016.08.004

Ben Ltaief, Y., Drira, Z., Hannachi, I., Bel Hassen, M., Hamza, A., Pagano, M., Ayadi, H., 2015. What are the factors leading to the success of small planktonic copepods in the Gulf of Gabes , Tunisia? J. Mar. Biol. Assoc. United Kingdom. https://doi.org/10.1017/S0025315414001507

Brewin, R. J., Dall'Olmo, G., Sathyendranath, S., & Hardman-Mountford, N. J. (2012). Particle backscattering as a function of chlorophyll and phytoplankton size structure in the open-ocean. Optics express, 20(16), 17632-17652.

D'Alimonte, D., Zibordi, G., Kajiyama, T., and Cunha, J. C.: Monte Carlo code for high spatial resolution ocean color simulations, Appl. Optics, 49, 4936, https://doi.org/10.1364/AO.49.004936, 2010.

Feinoltz, M., Johnson, B.C., Voss, K., Yarbrough, M., Flora, S. Immersion coefficient for the Marine Optical Buoy (MOBY) Radiance Collectors. Journal of Research of the National Institute of Standards and Technology, 122 (31). https://doi.org/10.6028/jres.122.031

Huot, Y., Morel, A., Twardowski, M. S., Stramski, D., & Reynolds, R. A. (2007). Particle optical backscattering along a chlorophyll gradient in the upper layer of the eastern South Pacific Ocean. Biogeosciences Discussions, 4(6), 4571-4604.

Malanotte-rizzoli, P., Manca, B.B., Ribera d'Alcalà, M, Bergamasco, A., Bregant, D., Georgopoulos, D., 1997. A synthesis of the Ionian Sea hydrography, circulation and water mass pathways during POEM-Phase I. Prog. Oceanogr. 39, 153–204.

Morel, A., Antoine, D., & Gentili, B. (2002). Bidirectional reflectance of oceanic waters: accounting for Raman emission and varying particle scattering phase function. Applied Optics, 41(30), 6289-6306.

Mueller, J. L. and Austin, R. W.: Ocean Optics Protocols for Sea- WiFS Validation, Revision 1, in: SeaWiFS Technical Report Se- ries, NASA Technical Memorandum 104566, Vol. 25, edited by: Hooker, S. B., Firestone, E. R., and Acker, J. G., Goddard Space Flight Center, Greenbelt, 1995.

Pegau, S., J. Zaneveld, B. Mitchell, J. Mueller, M. Kahru, J. Wieland, and M. Stramska, "Ocean optics protocols for satellite ocean color sensor validation, revision 4, volume IV: inherent optical properties: instruments, characterizations, field measurements and data analysis protocols," (National Aeronautical and Space administration, Goddard Space Flight Space Center, Greenbelt, Maryland 20771, 2003).

Pitarch, Jaime, Marco Bellacicco, Gianluca Volpe, Simone Colella & Rosalia Santoleri (2016) Use of the quasi-analytical algorithm to retrieve backscattering from in-situ data in the Mediterranean Sea, Remote Sensing Letters, 7:6, 591-600, DOI: 10.1080/2150704X.2016.1171922

Roether, W., Klein, B., Beitzel, V., Manca, B.B., 1998. Property distributions and transient-tracer ages in Levantine Intermediate Water in the Eastern Mediterranean. J. Mar. Syst. 18, 71–87.

Sullivan, J. M., M. S. Twardowski, J. Ronald, V. Zaneveld, and C. C. Moore, "Measuring optical backscattering in water," in Light Scattering Reviews 7: Radiative Transfer and Optical Properties of Atmosphere and Underlying Surface (Springer Berlin Heidelberg, Berlin, Heidelberg, 2013), pp. 189-224.

Thuillier, G., Labs, D., Foujols, T., Peetermans, W., Gillotay, D., Si- mon, P. C., and Mandel, H.: The solar spectral irradiance from 200 to 2400nm as measured by the SOLSPEC spectrometer from the ATLAS and EURECA missions, Sol. Phys., 214, 1–22, https://doi.org/10.1023/A:1024048429145, 2003.

Volpe, G., Colella, S., Forneris, V., Tronconi, C., and Santoleri, R.: The Mediterranean Ocean Colour Observing System – system development and product validation, Ocean Sci., 8, 869–883, https://doi.org/10.5194/os-8-869-2012, 2012.

Volpe, G., Colella, S., Brando, V., Forneris, V., La Padula, F., Di Cicco, A., Sammartino, M., Bracaglia, M., Artuso, F., Santoleri, R., 2019. Mediterranean ocean colour Level 3 operational multi-sensor processing. Ocean Sci. 15, 127–146. https://doi.org/https://doi.org/10.5194/os-15-127-2019.

Zhang, X., & Hu, L. (2009). Estimating scattering of pure water from density fluctuation of the refractive index. Optics express, 17(3), 1671-1678.

Zibordi, G., D'Alimonte, D., and Berthon, J. F.: An evaluation of depth resolution requirements for op- tical profiling in coastal waters, J. Atmos. Ocean. Tech., 21, 1059–1073, https://doi.org/10.1175/1520-0426(2004)021<1059:AEODRR>2.0.CO;2, 2004.

Zibordi, G., Berthon, J. F., Mélin, F., and D'Alimonte, D.: Cross- site consistent in situ measurements for satellite ocean color ap- plications: The BiOMaP radiometric dataset, Remote Sens. Envi- ron., 115, 2104–2115, https://doi.org/10.1016/j.rse.2011.04.013, 2011.

Zibordi, G., Melin, F., Talone, M. System Vicarious Calibration for Copernicus Ocean Colour Missions. 2017. JRC Technical reports. doi:10.2760/145183

Zibordi, G. and Ferrari, G. M.: Instrument self-shading in underwa- ter optical measurements: experimental data, Appl. Optics, 34, 2750–2754, https://doi.org/10.1364/AO.34.002750, 1995.